Click Here for Full Article

An observational and numerical study of a regional-scale downslope flow in northern Arizona

L. Crosby Savage III,[1] Shiyuan Zhong,[1] Wenqing Yao,[1] William J. O. Brown,[2] Thomas W. Horst,[2] and C. David Whiteman[3]

[1]   Boundary layer observations taken during the METCRAX field study in October of 2006 near Winslow in Northern Arizona revealed the frequent presence of a near-surface wind maximum on nights with relatively quiescent synoptic conditions. Data from a sodar, a radar wind profiler, several surface stations, and frequent high-resolution rawinsonde soundings were used to characterize this boundary layer wind phenomenon and its relation to synoptic conditions and the ambient environment. The data analyses are augmented by high-resolution mesoscale numerical modeling. It is found that the observed nocturnal low-level wind maximum is part of a regional-scale downslope flow converging from high terrain of the Colorado Plateau toward the Little Colorado River Valley. The depth of this downslope flow is between 100 and 250 m with a peak speed of $4-6$ m s^{-1} occurring usually within the lowest 50 m above ground. Opposing ambient winds lead to a longer evening transition period, shallower slope flows, and a smaller horizontal extent as compared to supporting synoptic winds. A simple analytical solution based on local equilibrium appears to agree fairly well with the observed layer mean downslope wind speed, but the classic Prandtl solution for maximum downslope wind speed fails to match the observations. The properties of the flow appear to be insensitive to changes in soil moisture, land cover, and surface roughness length. The contribution to the low-level wind maximum by inertial oscillation at night is found to be insignificant.

1. Introduction

[2]   Terrain-induced local or regional circulations are quite common within the western United States due to the complex topography and the climatologically dry stable conditions of the region. These terrain-induced flows have previously been observed along valley sidewalls [*Whiteman*, 1982], within basins [*Clements et al.*, 2003], and down mountain slopes [*Horst and Doran*, 1986]. Such observations lead to important discoveries of the characteristics and consequences of downslope flows within all types of topographic environments. *Alexandrova et al.* [2003] found a striking correlation between the thermally driven slope flow around Salt Lake City, UT and the fluctuation of aerosol particles of diameter less than 10 microns within the city. A similar study in Mexico City found that a nocturnal downslope flow was the main cause of an increase in ozone concentrations within the heavily populated urban area [*Raga et al.*, 1999]. *Smith et*

al. [1997] has pointed to the consequences of slope flows as an obstacle in transportation management, land use planning, and air pollution management for determining the environmental and economical impacts upon a region.

[3]   Observational studies have shown the characteristics of nocturnal downslope flows vary with slope angle, slope length, surface type, ambient winds, and stability. Many investigators have used analytical and numerical models to characterize the structure and evolution of downslope flows and to relate them to the ambient or large scale atmospheric conditions. *Prandtl* [1942] was one of the first to develop a theoretical model for describing the vertical structure of downslope flow. Prandtl's model gives the height and speed of the downslope jet as a function of the stability, slope angle, and eddy diffusivity. *Mahrt* [1982] examined the forcing mechanisms behind downslope flows by carefully evaluating the relative roles of terms in the momentum and thermodynamic equations in a slope following coordinate. These analytical studies have provided a basis for understanding the different observed characteristics of downslope flows in different environments.

[4]   Recent studies have focused more on the interaction of downslope flow with dynamical forces at different scales. Idealized numerical simulations have examined the impact of slope shape. *Smith and Skyllingstad* [2005] found that

[1]Department of Geography, Michigan State University, East Lansing, Michigan, USA.
[2]Earth Observing Laboratory, National Center for Atmospheric Research, Boulder, Colorado, USA.
[3]Department of Meteorology, University of Utah, Utah, USA.
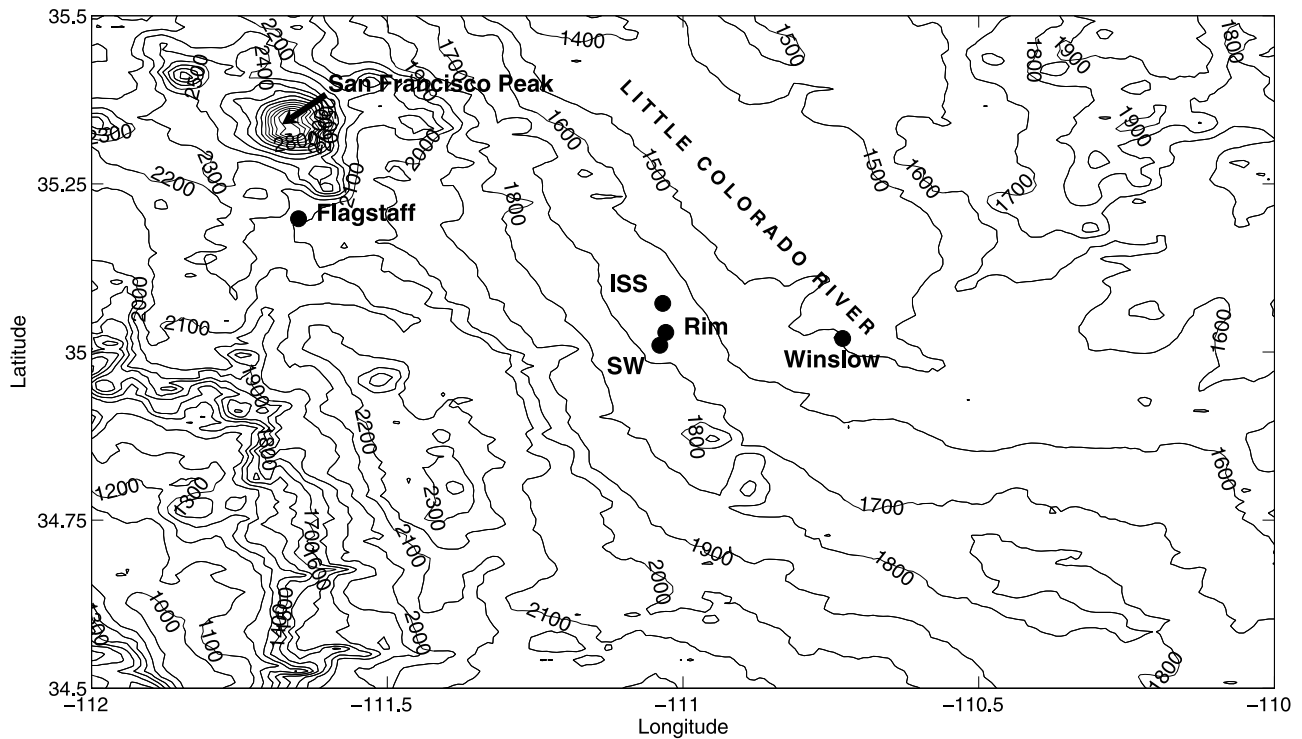
Figure 1. Topographic map of the study region indicating the locations of the observational sites.

slopes with a concave shape have a stronger acceleration near the top of the slope which then transitions toward a slower more elevated jet near the base. Uniform slopes, on the other hand, were found to maintain a constant profile of downslope flow along the slope, with stronger accelerations near the base. Other idealized studies have demonstrated the importance of inhomogeneous surface parameters along the slope [*Shapiro and Fedorovich*, 2007], and the impact of opposing synoptic scale flow, which affects the depth and strength of the downslope flow [*Arritt and Pielke*, 1986]. Along with these idealized studies, observational and laboratory studies have examined downslope flows over small slopes [*Soler et al.*, 2002], slope discontinuities [*Fernando et al.*, 2006], the impact of downslope flow upon turbulence [*Van Der Avoird and Duynkerke*, 1999; *Monti et al.*, 2002], and the interaction of downslope flows with larger scale phenomena, such as mountain waves [*Poulos et al.*, 2000]. While analytical, numerical, and laboratory studies have aided the understanding of downslope flow, field observations have provided a vital validation to theoretical findings. Previous observational studies have been carried out over isolated small-scale slopes only a few kilometers in length [*Doran et al.*, 2002; *Horst and Doran*, 1986; *Haiden and Whiteman*, 2005], or at larger scales in the pole regions of Antarctica [*Renfrew and Anderson*, 2006; *Heinemann and Klein*, 2002]. This has lead to a limited understanding of downslope flows along larger scale slopes and their interactions with synoptic forcing in midlatitude regions.

[5] In October 2006, the Meteor Crater Experiment, or METCRAX, was launched to investigate the evolution of the stable boundary layer and the formation of atmospheric seiches in Arizona's Meteor Crater approximately 60 km east southeast of Flagstaff, AZ. Observations were made both inside and outside Meteor Crater to document the interaction of the temperature structure and wind inside the crater with the ambient flows and stability conditions. Observations outside the Meteor Crater found frequent near-surface nocturnal wind maxima ($4-6$ m s^{-1}). These nocturnal near-surface wind maxima were associated with southwesterly winds which, based on the topography at the site, were likely to be downslope flows. Little is known, however, about the horizontal extent or scale of this downslope flow, its evolution with time, its depth, and how its characteristics, such as onset time, peak speed, depth etc., change with synoptic conditions. The METCRAX observations afforded a unique opportunity to answer these questions. This paper combines METCRAX observations with a mesoscale numerical model to characterize this wind phenomenon and its interaction with larger-scale forcing. Section 2 describes in more detail the site and measurements while section 3 describes the relevant observations. Section 4 introduces numerical model simulations and their results. Finally, conclusions are drawn in section 5.

2. Sites, Instrumentation, and Measurements

[6] The METCRAX observations were concentrated at the Meteor Crater (35.07 N, 111.03 W) 30 km west of Winslow, Arizona (Figure 1). The site ($\sim$1600 m above mean sea level or MSL) is near the Little Colorado River Valley with topography sloping upward to the west-southwest to the higher terrain of the San Francisco Peaks (southeast of Flagstaff and about 2200 m MSL). The approximately 2% slope is more or less homogeneous over a 110 km-long distance. Vegetation along the sloping terrain changes considerably with elevation. Ponderosa pines and juniper woodlands cover the higher elevations. At lower elevations, an increase in temperature and lack of moisture limit the
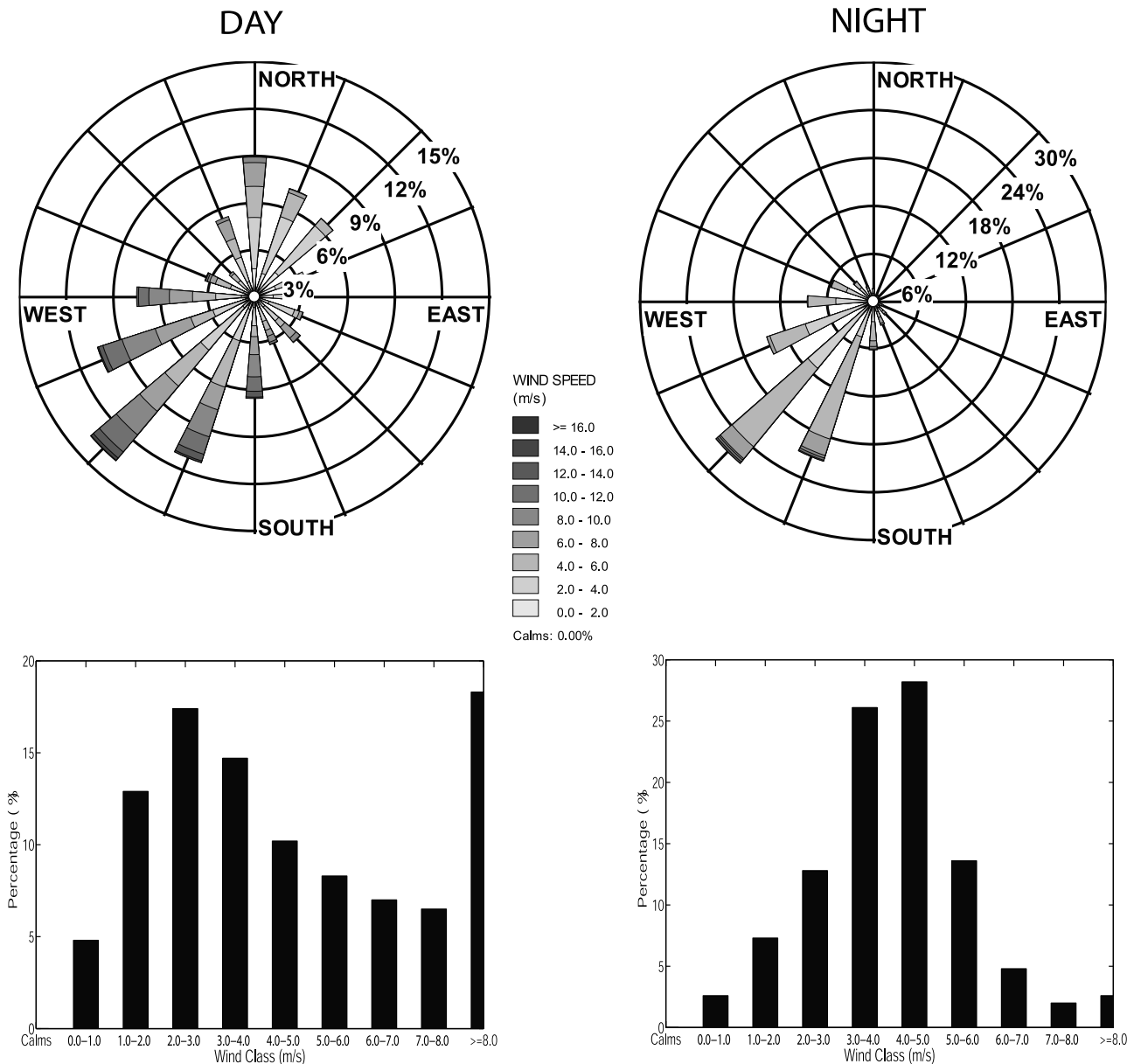
Figure 2. Wind roses and frequency distributions for the 10-m wind at the ISS site for October 2006.

vegetation to prairie grassland and small desert shrubs. Climate within the region is typical of much of the southwestern United States, which is dominated by subsidence from high pressure ridging more than 70% of days in both summer and early fall seasons [*Wang and Angell*, 1999]. This climatic pattern of clear, stable conditions makes the region especially susceptible to terrain-induced circulations.

[7] To accurately observe the circulation along the slope, three observational sites were installed at various locations. The first was 5 km north-northwest of Meteor Crater. This site was equipped with the National Center for Atmospheric Research (NCAR)'s Integrated Sounding System (ISS), which consisted of an enhanced surface weather station, a 915-MHz radar wind profiler with Radio Acoustic Sounding System (RASS), and a rawinsonde sounding system. Vaisala RS-92 GPS sondes were launched on seven Intensive Observational Periods (IOPs) during the month-long experiment and the launches would start at 1500 LST and

continue until 0900 LST the next morning at 3 hourly intervals. This site will hereafter be referred to as the ISS site. A second measurement site (henceforth designated the SW site) was located 2.5 km southwest of Meteor Crater. The site had a 10-m weather tower and a mini Sodar (Metek DSDPA.90-24) with RASS that measured wind speed and direction and temperature continuously from 40 m above ground to about 200 m aloft at 20 m vertical resolution. The third site was on the northwest rim of Meteor Crater (henceforth Rim site) where a 10-m tripod was installed with temperature and humidity sensors (Vaisala 50Y) mounted at two levels (2 m and 10 m) and a R. M. Young propeller vane wind monitor at the 10 m level.

[8] The general behavior of near-surface winds during the month-long experiment can be seen by the wind roses and frequency distribution at the ISS site for the entire month of the experiment in Figure 2 for both nighttime and daytime. Dominating the nighttime period over fifty percent of the
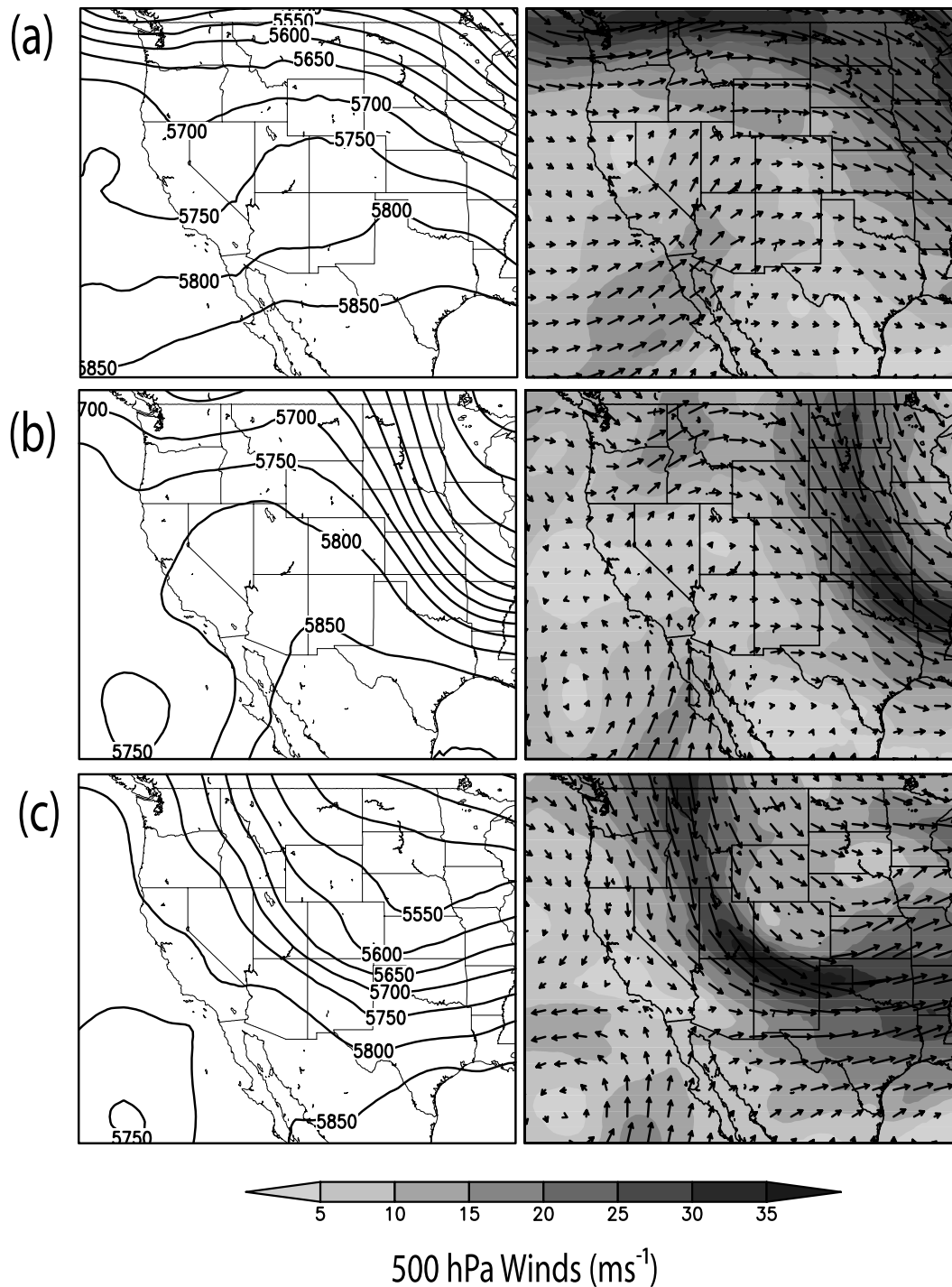
Figure 3. 0500 LST 500-mb geopotential height fields and wind vectors for (a) IOP 6, 29 October, (b) IOP 5, 23 October, and (c) IOP 4, 21 October, based on North American Regional Reanalysis (NARR) data.

time is a terrain-following southwesterly flow with a frequent speed of 4 to 5 m s^{-1}. The daytime period also shows a high frequency from the southwest, though a small peak from the north-northeast possibly exemplifies the effects of a weak upslope component. Strong surface winds exceeding 8 m s^{-1} were caused by downward mixing of strong synoptic winds during daytime.

[9] In this study, surface and upper air observations from three of the seven METCRAX IOPs (IOP 4, 5, 6) are used to investigate the detailed characteristics of the nocturnal downslope flow and its interactions with synoptic conditions. The three IOPs were selected to provide a range of different synoptic wind directions and speeds.

3. Observed Downslope Flow Characteristics

3.1. Synoptic Conditions

[10] The synoptic conditions for the three IOPs are described in this section. IOP 6 (28–29 October) was
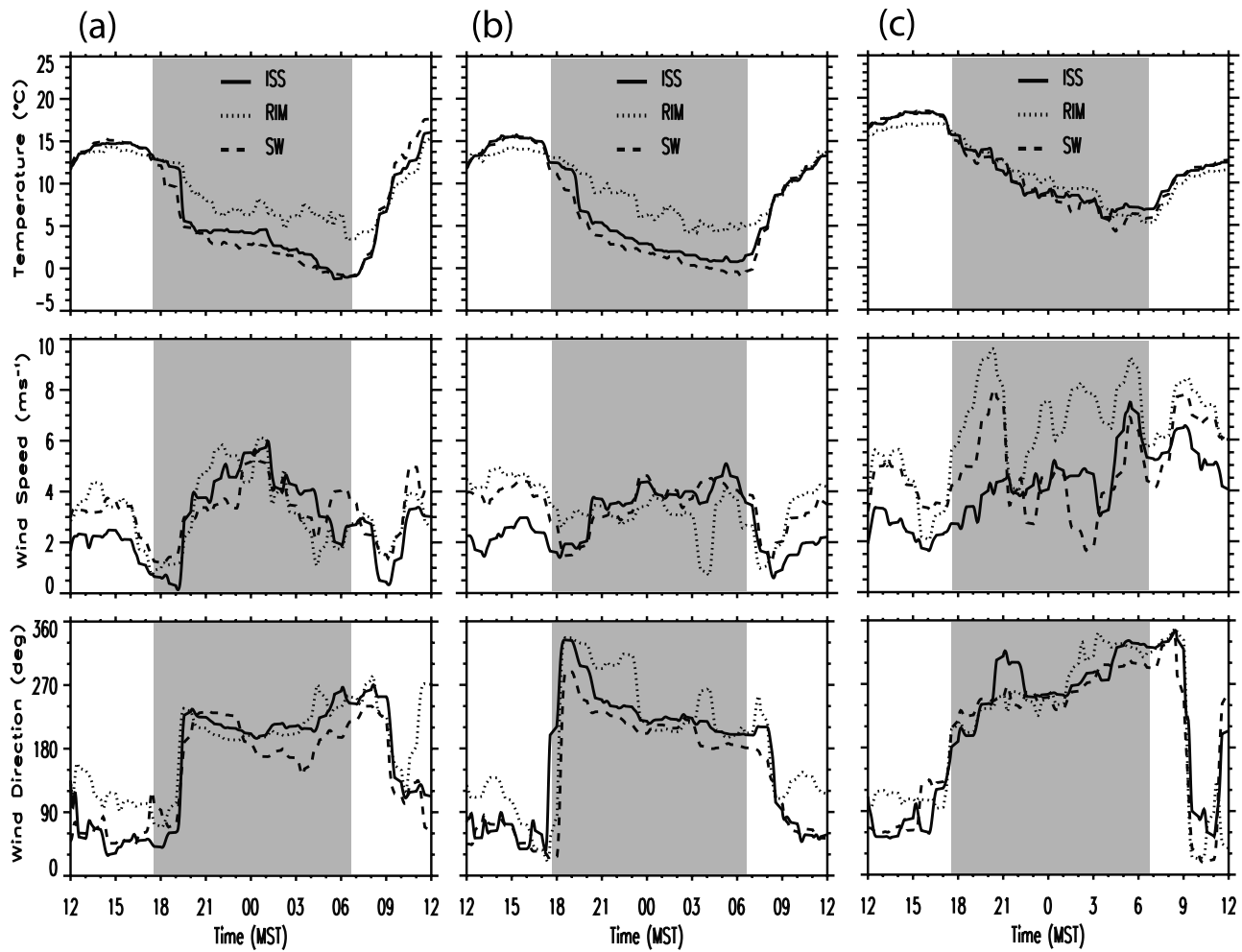
Figure 4. Time series of surface temperature, wind speed, and wind direction at ISS, RIM, and SW sites for (a) IOP 6, 28−29 October, (b) IOP 5, 22−23 October, and (c) IOP 4, 20−21 October.

characterized by weak ambient winds from the southwest, allowing downslope flow to develop over the region. Synoptic conditions were dominated by a ridge of high pressure between a digging trough in the Great Plains and a weak cutoff low-pressure system off the coast of California (Figure 3a). This allowed weak winds aloft to develop over northern Arizona through most of the night before giving way the next morning to a southerly jet. The weak ambient winds were typical of downslope development throughout the month, though the ambient wind direction was not always from the southwest.

[11] IOP 5 (22−23 October) was characterized by a low-level easterly jet, or opposing ambient wind to the southwesterly downslope flow. The easterly flow occurred as a low level jet between 700 and 900 m above ground level as the cutoff low aloft pushed a surface trough into Northern Arizona (Figure 3b). Above the easterly wind layer and similar to IOP 6, the synoptic winds aloft at 500 hPa were relatively weak at 5 to 10 m s^{-1} from the south or southwest (Figure 3b). This easterly low-level jet opposes the southwesterly downslope flow, contributing to the differences in the observed downslope flows between this night and the night of IOP6 when the midlevel large-scale winds were in the same direction as the downslope flow.

[12] As synoptic conditions aloft strengthened and strong winds began to mix down to the surface, the signatures of terrain-induced circulations became weaker and sometimes disappeared all together. An example of synoptic forcing overpowering local forcing is given in IOP 4 (20−21 October) in Figure 3c. On this night, a digging trough developing just to the north of the region brought strong northwesterly winds to the study area. The strong winds began to mix to the surface, which limited the impact of the terrain-induced circulation.

3.2. Time Variations of the Downslope Flow

[13] Observations taken from the three sites illustrate the downslope flow characteristics (Figure 4). During IOP 6 (Figure 4a), the transition in the evening from northeasterly (i.e., upslope) to southwesterly flow is abrupt and exhibits a continuous anticyclonic turn toward the southwest. Accompanying the hour long transition was a steep drop in temperature of approximately 7 °C, which was a result of near calm wind and clear conditions allowing effective cooling through radiation loss. After the evening transition, surface winds increased to 4 to 5 m s^{-1} and remained steady from the southwest until 0930 LST the next morning. The morning transition back to northeasterly flow is just as
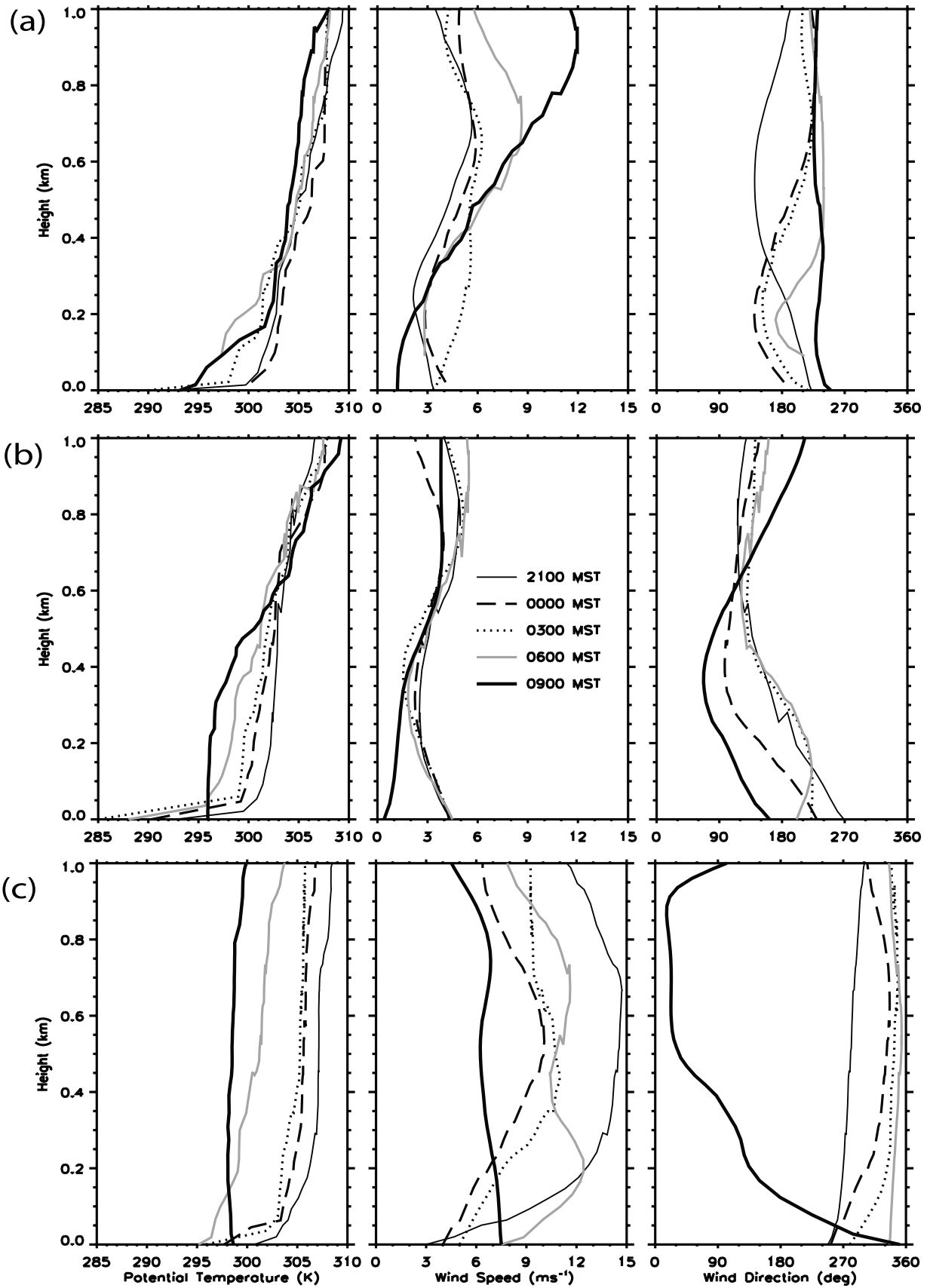
Figure 5. Vertical profiles of potential temperature, wind speed, and wind direction at the ISS site for (a) IOP 6, 28–29 October, (b) IOP 5, 22–23 October, and (c) IOP 4, 20–21 October.
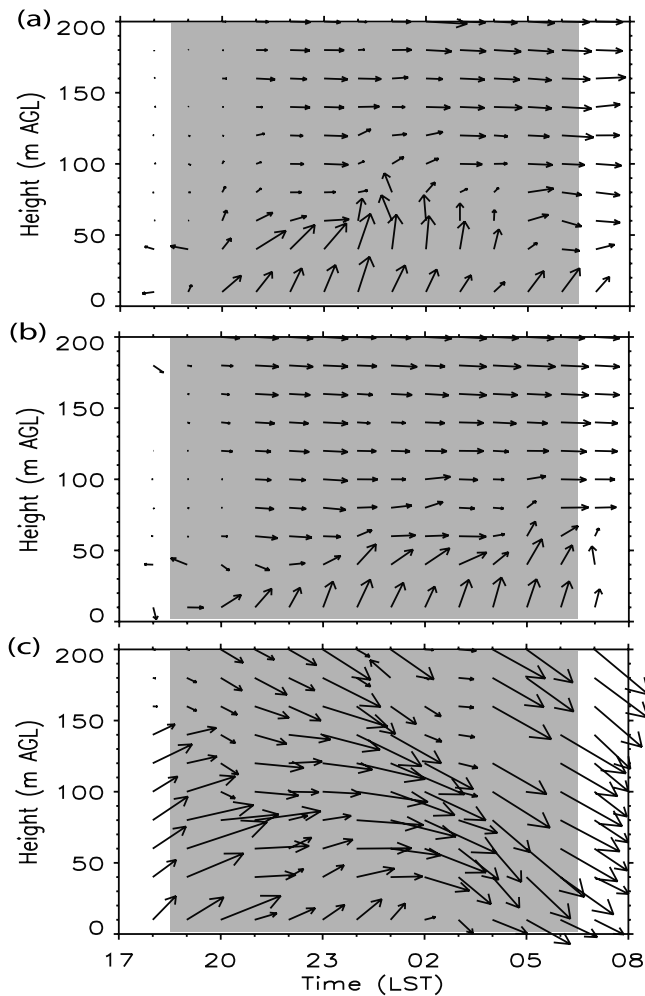
Figure 6. Hourly wind vectors from the Sodar and surface observations at the SW site for (a) IOP 6, 1800 LST 28 October – 0700 LST 29 October (b) IOP 5, 1800 LST 22 October – 0700 LST 23 October, and (c) IOP 4, 1800 LST 20 October – 0700 LST 21 October.

abrupt as the onset of the downslope flow; occurring within an hour and accompanied with weak surface winds.

[14] Surface observations taken from IOP 5 show similar patterns to those observed during IOP 6 with a change in wind direction after sunset to the southwest (Figure 4b). The main difference between the supporting ambient flow of IOP 6 and the opposing ambient flow of IOP 5 was the evening transition period. The evening transition of IOP 5 took two hours longer than IOP 6 and exhibited a cyclonic shift, turning continuously from easterly flow during the day to northerly, and finally stopping with a southwesterly downslope flow. This agrees with the theoretical model findings of *Fitzjarrald*'s [1984] of delayed onset time with opposing ambient flow. The longer transition was also accompanied by weak winds near the surface and a temperature decrease of near 7 °C. Overnight, the surface winds were again characterized by a steady flow from the southwest averaging 4 m s^{-1}. The morning transition back to synoptically driven or possibly upslope flow, exhibited the

same characteristics as in IOP 6, though the transition occurred slightly earlier at 0810 LST.

[15] IOP 4 exhibited a shift in wind direction at the surface from easterly during the day to westerly at night, but the characteristics of the transition and flow are not comparable to the previous downslope flow examples (Figure 4c). Instead, the easterly winds during the day began to transition to a southwest direction before sunset. During previous IOPs, the downslope transition was accompanied by a decrease in near-surface wind speed and a rapid drop in temperature, but for IOP 4 the evening transition was characterized by increasing wind speeds and little temperature change near the surface. As the night progressed, the winds continued to slowly shift more westerly and eventually, after 0300 LST, became northwesterly, which was the same as the ambient flow direction aloft. Surface wind speeds during the period were also stronger and more variable in magnitude ranging from near 4 m s^{-1} to almost 10 m s^{-1}. The strong synoptic forcing is thus driving the surface winds, limiting the impacts of the terrain-induced circulation.

3.3. Vertical Structure of the Downslope Flow

[16] The vertical structure of the downslope flow was determined from 3-hourly rawinsonde soundings from the ISS site and from 1-h mean sodar observations at the SW site. Figure 5a illustrates the time sequence of the IOP 6 soundings, which were characterized by stable conditions aloft and a strong surface temperature inversion in the lowest 20 to 30 m above ground level (AGL) from 2100 LST on 28 October till 0600 LST the next morning. Accompanying the inversion was a near-surface wind maximum of 4 to 5 m s^{-1}, with wind speed weakening with height up to 200 m AGL. During the morning transition (around 0900 LST) the near-surface wind maximum disappeared as a growing convective boundary layer eroded the overlying temperature inversion and began to exhibit greater influence from larger scale forcing. From the
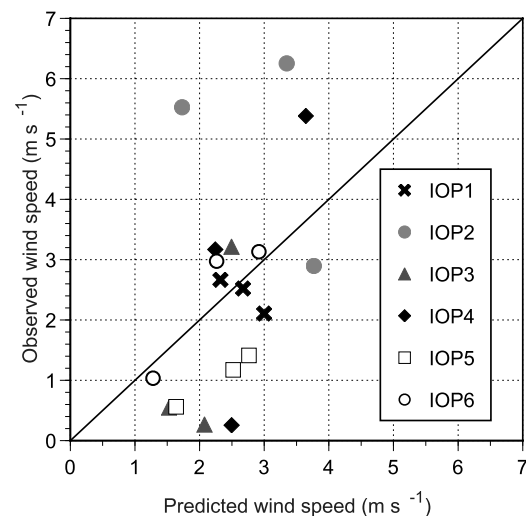
Figure 7. Comparison of observed layer-averaged downslope wind speed by the rawinsonde soundings at the ISS site with those predicted by the analytical equilibrium solution.

rawinsonde profile, it is difficult to determine the downslope flow layer depth, but the combined hourly sodar and 10-m surface observations taken at the SW site provide a detailed picture of the change in downslope flow depth during the night (Figure 6a). At first, the downslope flow was shallow and weak, but by midnight the depth and strength of the flow was at its peak. Consistent with the 0000 LST sounding, the southwesterly downslope flow extended up to 120 m AGL. Later in the night, the depth of the downslope flow began to decrease to below 100 m AGL, and after sunrise was limited to the first 10s of meters AGL. The fluctuation of the depth of the downslope flow throughout the night makes definitive determination of the height of the flow difficult, though a range of 50 to 150 m above AGL would best describe the downslope flow for IOP 6.

[17] The effect of easterly ambient winds on the downslope flow is illustrated through the series of three-hourly vertical sounding profiles taken during IOP 5 (Figure 5b). The soundings again showed a typical terrain-driven southwesterly flow with maximum speed close to the surface, and a strong inversion of almost 10 K just above the surface. The morning transition around 0900 LST was similar to IOP 6, as the winds near the surface were significantly weaker and increased with height. A closer examination of the sounding and sodar observations for IOP 5 shows a fluctuating depth between 50 and 100 m, with the maximum depth noticeably lower than that in IOP 6 (Figure 6b). Similar to IOP 6, though, is an increase in depth overnight from about 10 m at the beginning of the night, to about 70 m by 0200 LST.

[18] The effects of the strong synoptic northwesterly flow from IOP 4 are seen in the vertical profiles of the 3-hourly soundings (Figure 5c). Unlike the previous IOPs, there was no wind maximum near the surface, but instead the winds increased with height and were predominantly from the northwest. The temperature inversion on this night was also much weaker compared to the other nights. The sodar observations taken from IOP 4 illustrate the strong influence of the synoptic northwest flow, as there is little evidence of terrain-induced drainage flow at any depth throughout the night (Figure 6c).

3.4. Comparison With Analytical Solutions

[19] A number of analytical solutions have been proposed to describe the characteristics of downslope flows [*Manins and Sawford*, 1979; *Kondo and Santo*, 1988; *Nappo and Rao*, 1987; *Mahrt*, 1982]. Most of these are simplified solutions of the bulk momentum equation for downslope flows

$$\frac{\partial}{\partial t}h\bar{u} + \frac{\partial}{\partial x}h\overline{u^2} = \frac{g}{\theta_o}h\bar{\theta}\sin\alpha - \frac{g}{\theta_o}\cos\alpha\frac{\partial}{\partial x}h^2\bar{\bar{\theta}} + \tau_o - \tau_h \quad (1)$$

Equation (1) is obtained by integrating the momentum equation in a slope-following coordinate system

$$\frac{\partial u}{\partial t} + u\frac{\partial u}{\partial x} + v\frac{\partial u}{\partial y} + w\frac{\partial u}{\partial z} = -\frac{1}{\rho_o}\frac{\partial p}{\partial x} + g\frac{\theta}{\theta_o}\sin\alpha + fv - \frac{\overline{\partial w'u'}}{\partial z}$$

$$(2)$$
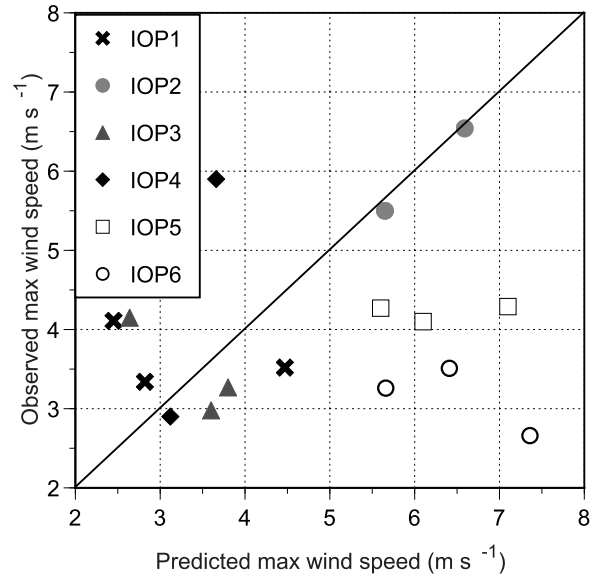
Figure 8. Comparison of observed maximum downslope wind speed observed by the 3-hourly rawinsonde soundings at the ISS site with those predicted by the Prandtl solution.

from the ground surface to the top of the slope flow layer with the assumption that hydrostatic equilibrium $g\frac{\theta}{\theta_0}\cos\alpha = -\frac{1}{\rho}\frac{\partial p}{\partial z}$ exits in the direction perpendicular to slope surface.

[20] In equation (1) and equation (2), u is the downslope wind component, α is the slope angle, h is the downslope flow depth, g is the gravity, θ_0 is the horizontally homogeneous basic state potential temperature, θ is the perturbation potential temperature or the heat deficit, and $\tau_0 - \tau_h$ is turbulent stress divergence across the slope flow layer, which is typically parameterized by $\tau_0 - \tau_h = -(C_D + k)\bar{u}^2$ with C_D being the surface drag coefficient and k the frictional force due to momentum exchange at the interface between the downslope flow layer and the ambient atmosphere. The overbar in equation (1) is the layer mean of a variable defined by $\bar{\varphi} = \frac{1}{h}\int_0^h \varphi(z)dz$; while the double bar is the layer mean of an integral from level z in the slope flow layer to the top of the layer, $\bar{\bar{\varphi}} = \frac{1}{h^2}\int_0^h dz\int_z^h \varphi(z')dz'$.

[21] A simple analytical solution for downslope wind speed under the condition of local dynamical equilibrium was proposed by several investigators [*Ball*, 1956; *Kondo and Santo*, 1988; *Mahrt*, 1982]. Under local equilibrium, buoyancy is balanced by turbulent stress divergence and equation (1) is simplified to

$$\frac{g}{\theta_0}h\bar{\theta}\sin\alpha = (C_D + k)\bar{u}^2 \quad (3)$$

Solving for layer averaged wind speed gives

$$\bar{u} = \sqrt{\frac{g}{\theta_o}h\bar{\theta}\sin\alpha/(C_D + k)} \quad (4)$$

Grid 1
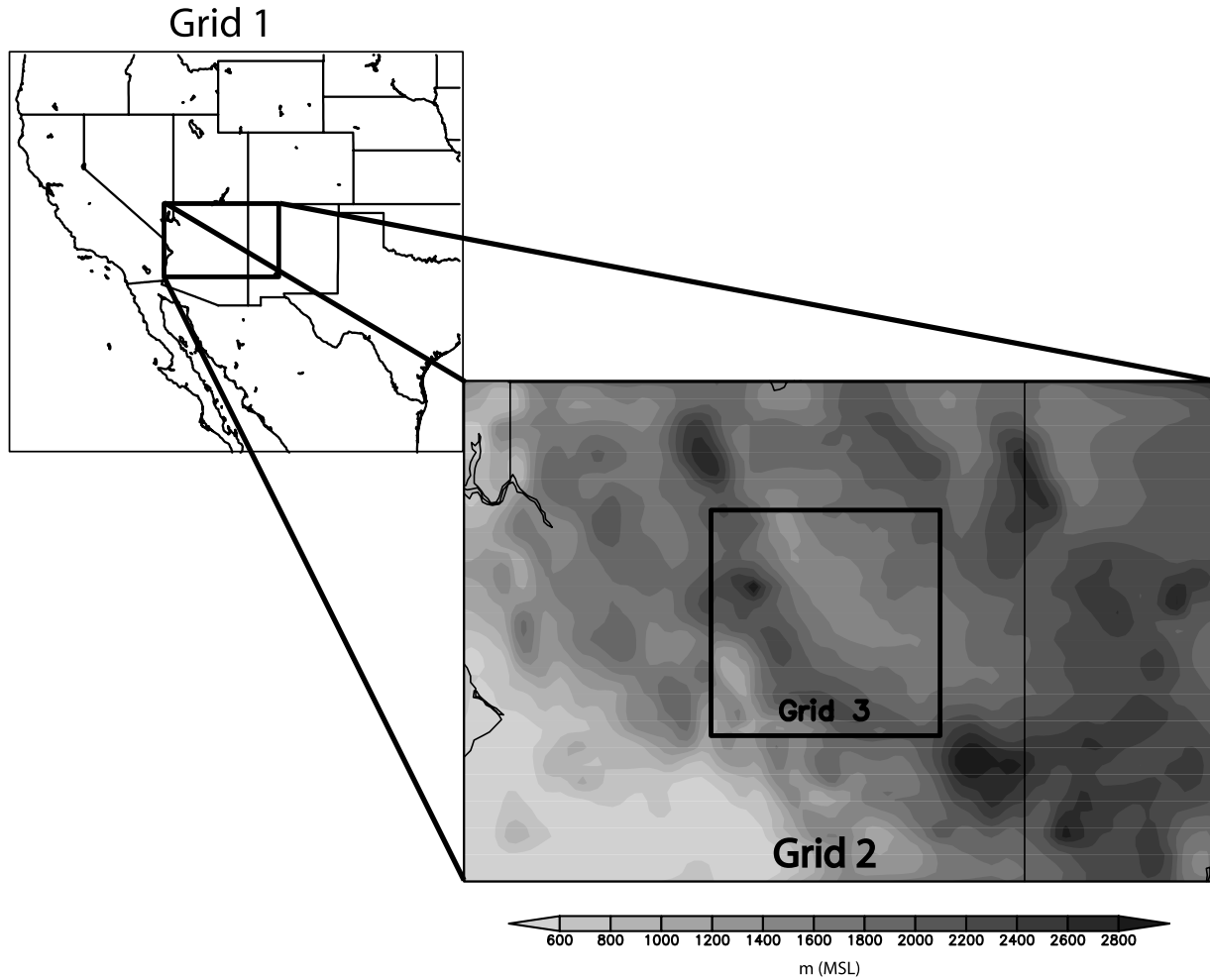
Figure 9. Location of the RAMS grids and the topography in the inner two grids.

Using nighttime radiosonde profiles launched from the ISS site during IOPs, the layer-averaged downslope wind speeds are estimated using equation (4) and the results are compared to those computed directly from the observed downslope wind components (Figure 7). A value of $C_D + k = 0.008$ is used in the computation to satisfy the assumption for local equilibrium that $F(C_D + k)/\sin \alpha = O(1)$ where F is the Froude number defined as $F = \frac{\bar{u}^2}{g'h}$ with $g' = g\frac{\bar{\theta}}{\theta_0}$ being the reduced gravity indicating the relative importance of transport and Coriolis force terms compared to the buoyancy and thermal wind term. The comparison shows that except for the two disturbed IOPs (IOP 2 and IOP 4) when the ambient winds became relatively strong after midnight, the average downslope wind speeds predicted by the local dynamical equilibrium theory fairly agrees with the observed values. In addition to explaining the differences between IOPs, the analytical solution also captures the variations within IOP 5 and IOP 6, which were the two best IOPs with quiescent synoptic conditions and well-developed downslope flows. The results here indicate that under weak synoptic forcing, the observed downslope flows were governed largely by local equilibrium between the buoyancy force associated with the temperature deficit and turbulent friction. Nocturnal downslope winds observed over a relatively uniform, low-angle slope (∼1.6°) in Salt Lake Valley were also found to be in local equilibrium [*Whiteman*

and Zhong, 2008; *Zhong and Whiteman*, 2008]. Under such circumstance, the simple analytical solution given by equation (4) may be used to predict the mean downslope wind speed.

[22] The rawinsonde observations were also used to evaluate the well-known *Prandtl* [1942] equilibrium solution for the maximum wind speed in downslope jets. Prandtl's solution employs eddy diffusivities and a simple thermodynamic equation where diffusion of heat is balanced by temperature advection associated with the basic state stratification. Under such an assumption, the maximum jet speed becomes linearly proportional to the temperature deficit at the surface, i.e.,

$$u_{\max} = 0.322\Delta\theta_{sfc}\sqrt{\frac{g}{\theta_0}\left(\frac{d\theta_0}{dz}\right)^{-1}\frac{K_h}{K_m}} \qquad (5)$$

where $\Delta\theta_{sfc}$ is the surface potential temperature deficit, θ_0 represents ambient potential temperature, and K_h, K_m are eddy diffusivities for heat and momentum. equation (5) indicates that the speed of the downslope jet increases linearly with increasing temperature deficit at the surface and increases with weakening ambient stratification.

[23] Figure 8 shows a comparison of the observed maximum downslope wind speed and the estimated maximum
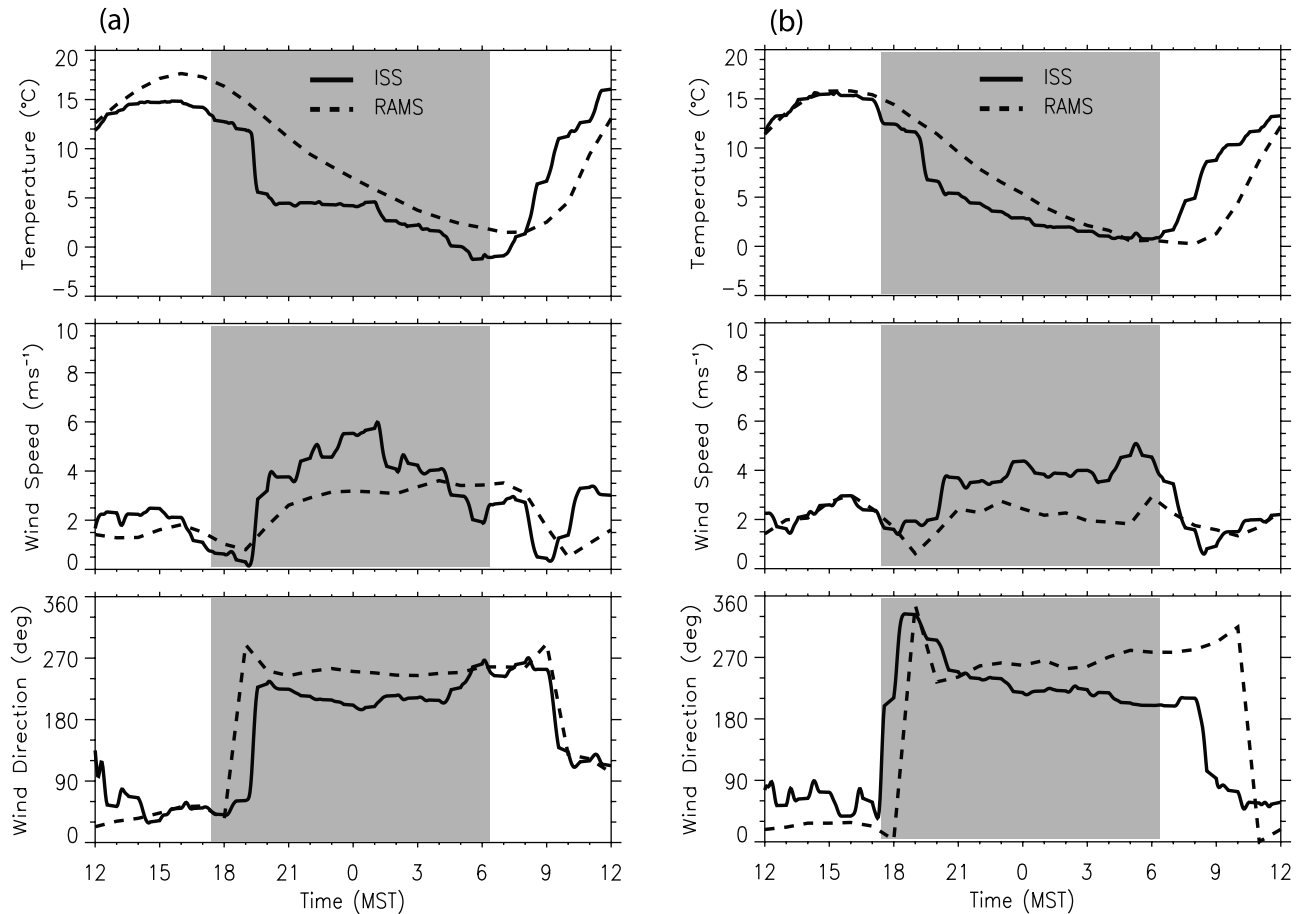
Figure 10. Comparison of simulated and observed surface temperature, wind speed and wind direction at the ISS site for (a) IOP 6, 28–29 October and (b) IOP 5, 22–23 October Nighttime period is indicated by the gray shading.

wind speed using the Prandtl solution described by equation (5) based on the nighttime rawinsonde soundings for IOPs 1–6. The calculation assumes that $K_h = K_m$ in equation (5). The plot shows relatively large scatter, suggesting that the Prandtl solution is not very accurate in predicting the observed downslope jet. It is interesting to note that the Prandtl solution appears to be in better agreement with observations during the disturbed IOP 2 than with the quiescent IOPs 5 and 6. For IOPs 5 and 6, the analytical values are consistently higher than the observed values. Detailed analyses indicate that the clear sky and near calm conditions during the nights of IOPs 5 and 6 allowed for strong radiational cooling on the ground and the lack of mixing limited the cooling to a very shallow layer. Consequently, the potential temperature deficit at the surface $\Delta\theta_{sfc}$ is very large, which leads to a much larger u_{max} than the actual observed jet maximum. A better agreement may be achieved by replacing the surface potential temperature deficit with an average value across a shallow near-surface layer.

4. Numerical Modeling

4.1. Model Setup

[24] The observations captured the temporal variation and the vertical structure of the downslope flows. Unfortunately, the observations were limited to a few closely located sites

and were unable to document the spatial extent of this downslope flow. To better examine the extent of the downslope flow beyond the limited observational sites, the Regional Atmospheric Modeling System (RAMS [*Pielke et al.*, 1992]), a nonhydrostatic primitive equation mesoscale model in a terrain-following coordinate system, was employed to simulate these IOPs. Subgrid-scale turbulent diffusion is parameterized using a level-2.5 scheme [*Mellor and Yamada*, 1982], which allows a turbulent exchange across the jet maximum and a smooth transition between stable and unstable regimes. Turbulent sensible and latent heat fluxes and momentum fluxes in the surface layer are evaluated based on the formulation of *Louis*'s [1979]. Radiative heating and cooling were represented by the *Chen and Cotton* [1983] short- and long-wave radiation schemes, which consider the effect of clouds but do not include the effects of aerosols on radiation.

[25] To accurately represent both the synoptic forcing and local forcing within the region three two-way interactive nested grids with horizontal grid spacing of 32 km, 8 km, and 2 km were used. The outer grid contained most of the western United States and portions of Mexico and the Pacific Ocean, the second grid consisted of most of Arizona and western part of New Mexico, and finally, the innermost grid covers north-central Arizona including the Little Col-
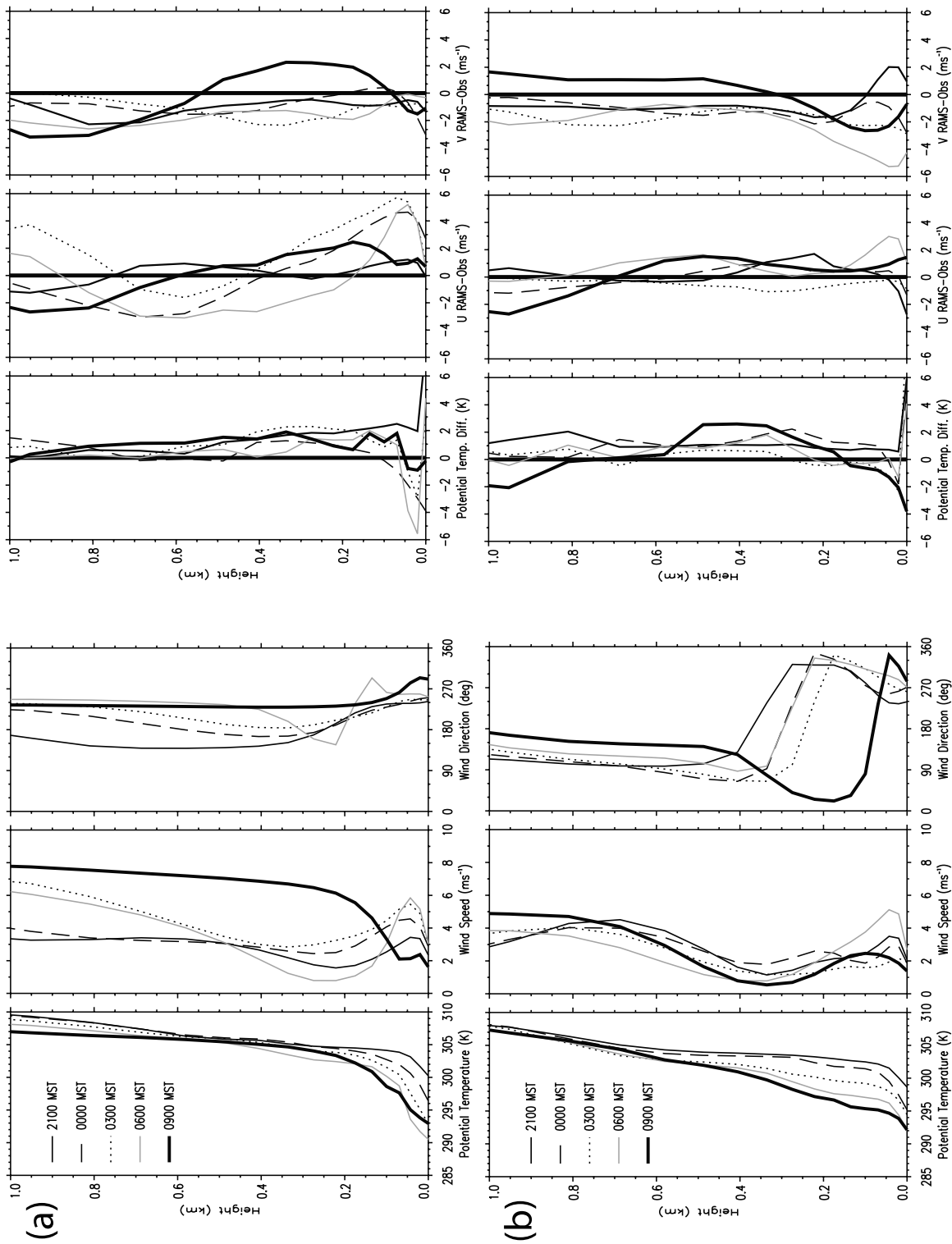
Figure 11. Simulated vertical profiles (left) of potential temperature, wind speed, and wind direction at the ISS site and difference (right) from observations of potential temperature, u wind, and v wind for (a) IOP 6, 28–29 October, (b) IOP 5, 22–23 October.

(a)   (b)
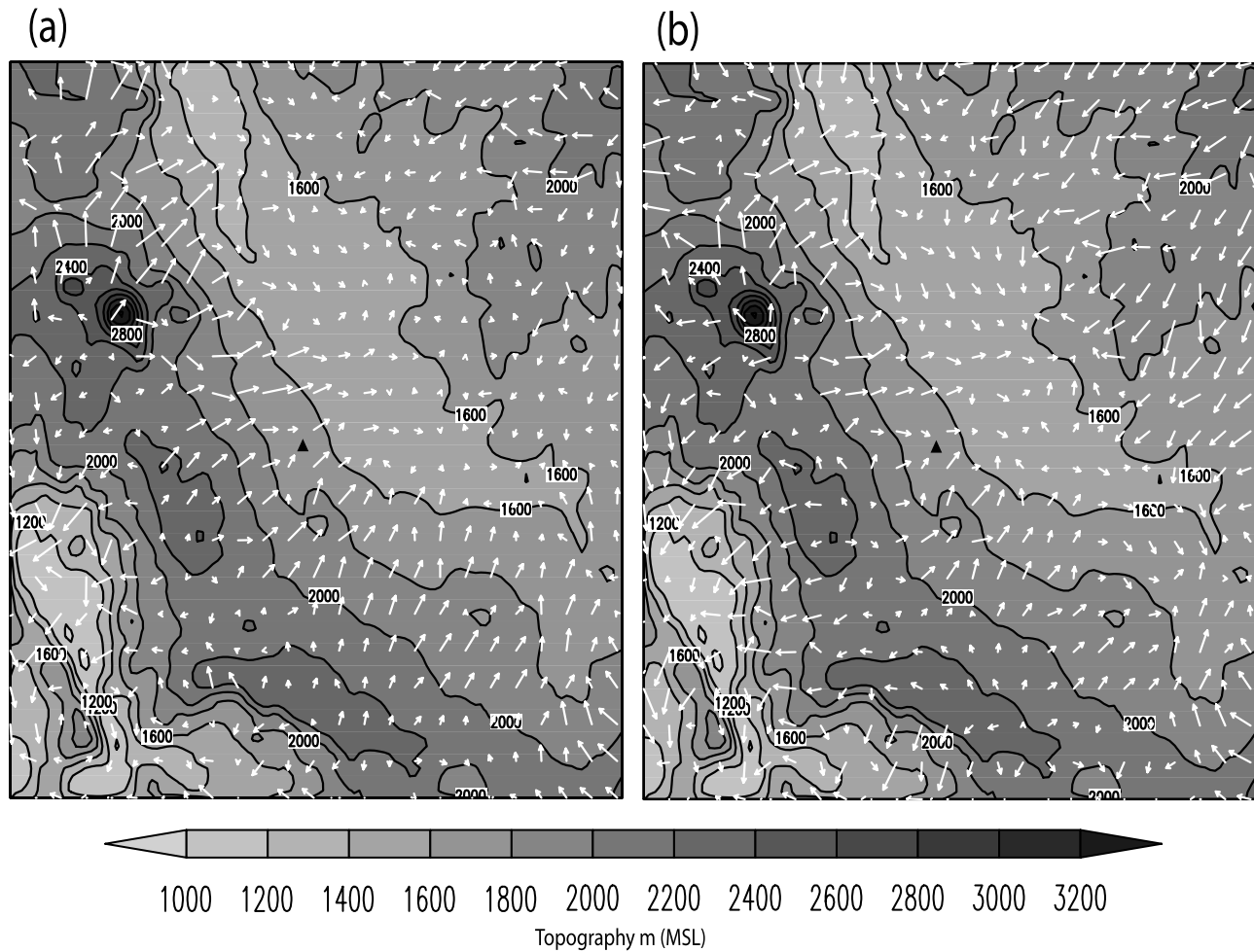
Figure 12. Simulated near-surface wind vectors and topography contours in the innermost grid for (a) IOP 6, 28–29 October (b) IOP 5, 22–23 October The triangle indicates the location of the ISS site.

orado River Valley and the 3800 m San Francisco Peaks (Figure 9). Each grid had 35 vertical levels, stretching from 20 m near the surface to 1000 m above 10 km. The simulations were initialized at 1200 UTC (0500 LST) using output from the National Center for Environmental Prediction (NCEP)'s North American Model (NAM) and each simulation ran for 31 h to end at 1900 UTC (1200 LST) the following day.

[26] The goal of the model simulations was to provide a more detailed look at the horizontal and vertical extent of the downslope flow and how its characteristics change from one day to the next. For this reason simulations were performed for the two best IOP nights, IOP 5 (22–23 October) and IOP 6 (28–29 October), when synoptic forcing was weak and the downslope flows were well developed.

4.2. Simulation Results and Discussion

[27] The simulated downslope flow characteristics were first compared with the observations for the two IOPs. As shown in Figure 10, the model was able to capture the major observed differences between the two IOPs. For IOP 6, the simulated evening and morning transitions occurred at the same time as observed and the simulated anticyclonic shift also occurred within an hour, as it did in the observations.

The evening transition of IOP 5 is also well simulated by the model, as the transitional period to downslope flow takes longer than IOP 6 and exhibits more of a cyclonic shift. The simulations also adequately captured the drop in wind speed at the surface at the time of transition to downslope for both IOPs, though the simulated near surface temperature was warmer than observed. After the transition the simulated wind speeds increased overnight, as observed, but were 1 m s^{-1} less than observations. The discrepancy between the simulated wind direction that was more westerly and the observed direction that was southwesterly may be attributed to the relatively coarse 30' DEM topography data set used by the simulations as well as the relatively coarse model grid resolution.

[28] Soundings taken from the two simulations are comparable to their observed counterparts at the ISS site (Figure 11). The simulated vertical structure and evolution of potential temperature are in good agreement with observations, although the simulated surface-based inversion is weaker in the model. Both the simulation and the observations show a low-level wind maximum with wind speed decreasing with height between 200 and 400 m and increasing above, but the observed wind maximum is near the ground while the simulated winds peak around 50 m above
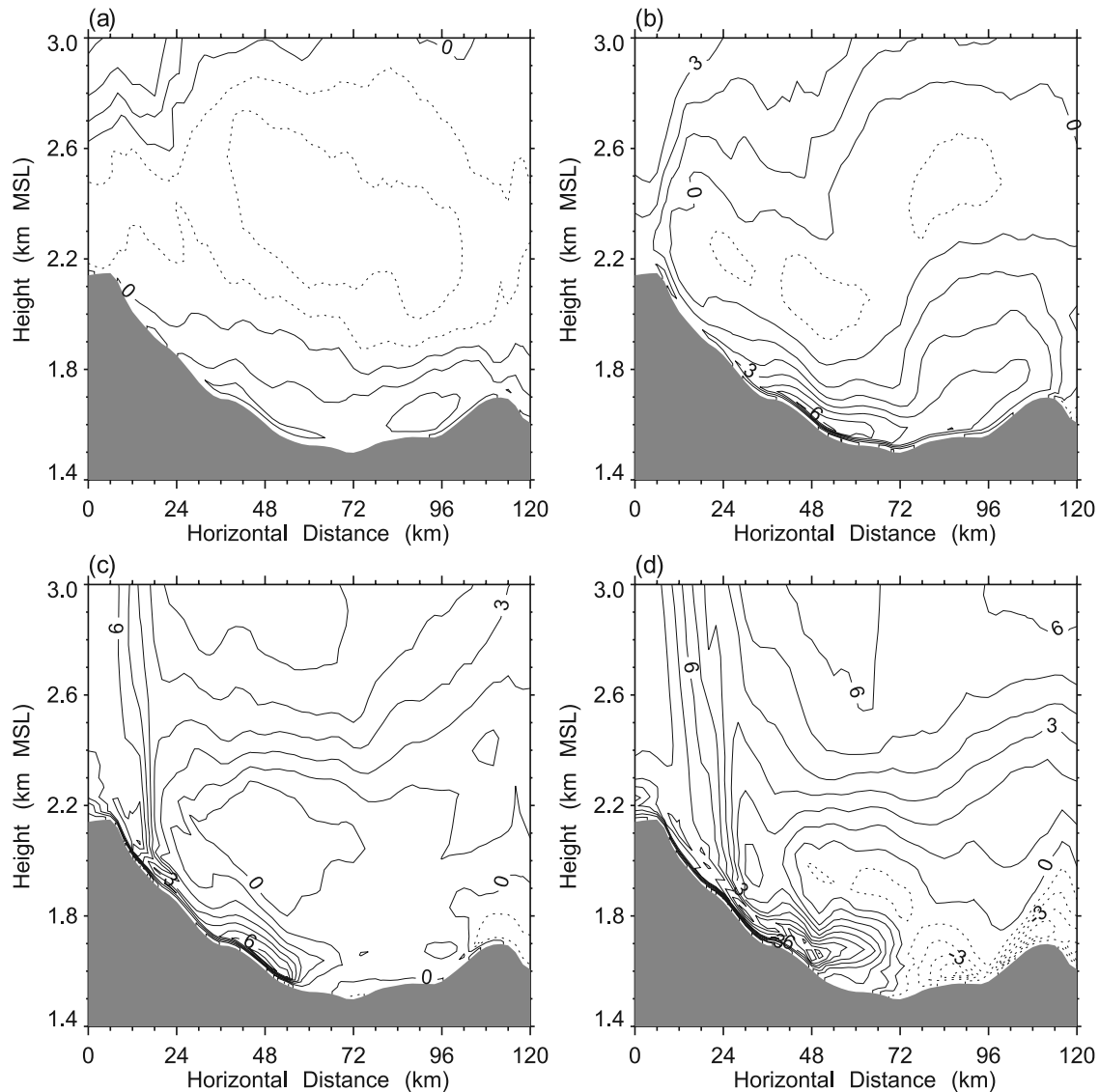
Figure 13. Simulated u wind components on an east-west vertical cross section through the ISS site at (a) 2100 LST, (b) 0000 LST, (c) 0300 LST, and (d) 0600 LST for IOP 6, 28–29 October.

the ground. The discrepancy between the observed and simulated height of the wind maximum can be attributed partially to relatively poor vertical resolution and partially to the tendency of RAMS to produce stronger mixing near the surface during nighttime [*Zhong and Fast*, 2003; *Berg and Zhong*, 2005; *Fast and Zhong*, 1998]. The vertical wind direction profiles are quite similar to the observations, though slight variations occur near changes of wind direction. IOP 6 is 100 m higher in representing the weak southerly wind seen at 200 m in the observations. IOP 5 has a better handle on the height of the change in wind direction, but the simulated results show a northern turn in wind direction with height as opposed to the more southerly turn that was actually observed.

[29] Figure 12 shows the simulated near-surface wind vectors in the innermost model domain at 0000 LST when the observations indicated fully developed downslope flows for both IOPs. The simulations also exhibit well-developed downslope flows at the observational sites and it is clear that

this observed downslope flow is part of regional-scale, diurnally varying terrain-induced circulation that converges from high terrains into the Little Colorado River Valley region at night and diverges out of the valley toward high terrain during daytime (not shown). The downslope flow in IOP 6 is noticeably stronger and extends further into the Little Colorado River Valley than IOP 5, which is hampered by stronger ambient flow and the easterly jet aloft. Also noticeable are the increased wind speeds on the other side of the valley, which may be enhanced by the easterly jet and may play a role in producing a smaller horizontal extent of southwesterly downslope flow for IOP 5.

[30] The simulated u-components on an east-west vertical cross section through the ISS site are shown in Figures 13–14 for four different times during the nights of IOPs 5 and 6. These cross sections clearly illustrate the vertical structure and the time variation of the downslope flows. There are significant differences in the vertical and horizontal extent of the downslope flows between IOP 5
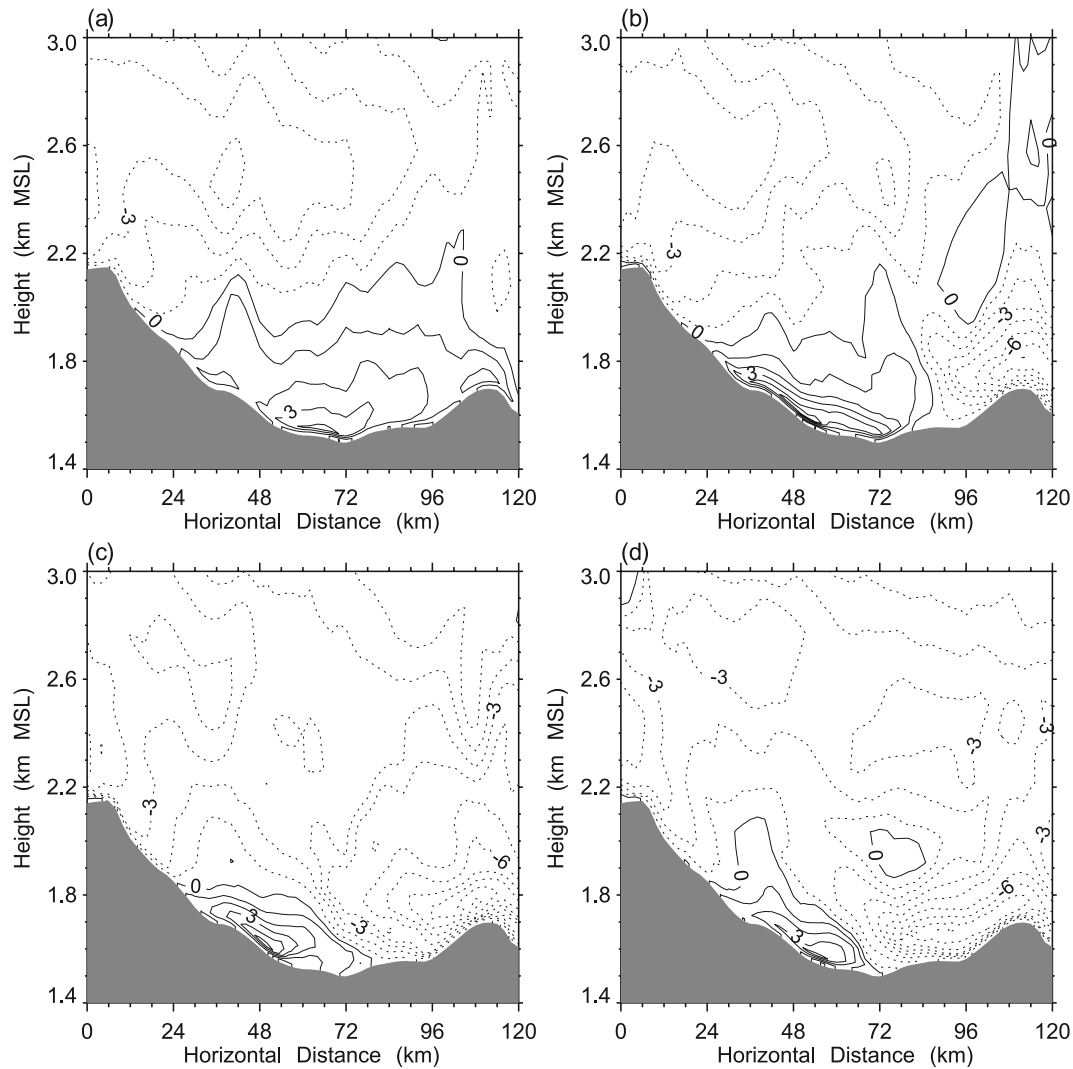
Figure 14. Simulated u wind components on an east-west vertical cross section through the ISS site at (a) 2100 LST, (b) 0000 LST, (c) 0300 LST, and (d) 0600 LST for IOP 5, 22–23 October.

and IOP 6, due primarily to the differences in the background wind direction. In the case of IOP 6 where the large-scale winds are west-southwesterly, the westerly downslope winds have a larger horizontal and vertical extent compared to IOP 5 when the midlevel background winds were easterly. The development of the downslope flow on the east side slopes of the Little Colorado River Valley is significantly delayed in IOP 6 and did not occur until early morning. In IOP 5, the easterly background winds allowed the downslope flow on the lower east side slope to develop at midnight and suppressed the advance of the downslope flows from the steeper west side slope. In addition to the differences in the structure of the winds, the stratification also appears to be stronger in the lower atmosphere over the sloping terrain in IOP 6 than in IOP 5 (not shown).

4.3. Sensitivity Experiments

[31] Additional simulations were performed for IOP 5 to examine the sensitivity of the characteristics of these regional scale downslope flows to several physical and environmental factors. The first factor is soil moisture, which has been shown to impact katabatic flows and is variable in Northern Arizona from seasonal rains [*McCumber and Pielke*, 1981; *Banta and Gannon*, 1995]. Two additional simulations were performed assuming drier (soil moisture 0.1) and wetter (soil moisture 0.35) soil compared to the moderate soil moisture value (0.2) used in the control simulation. The second factor is land cover. In the control simulation, the land cover is heterogeneous with a mixture of grassland and small shrubs at lower elevations and ponderosa pines and juniper woodlands at higher elevations. Variations in vegetation type or land cover have been found to change the strength of downslope flows [*Sun et al.*, 2006], and so an additional numerical experiment was performed using homogeneous land cover with semidessert in the middle and inner grids. Potential impact of surface friction on the downslope flow was examined by changing the surface roughness from the control simulation of $z_0 = 0.01$ m to $z_0 = 0.05$ m. An experiment was designed to investigate the effect of Coriolis force on the current regional-scale (~100 km) downslope flows. Coriolis force
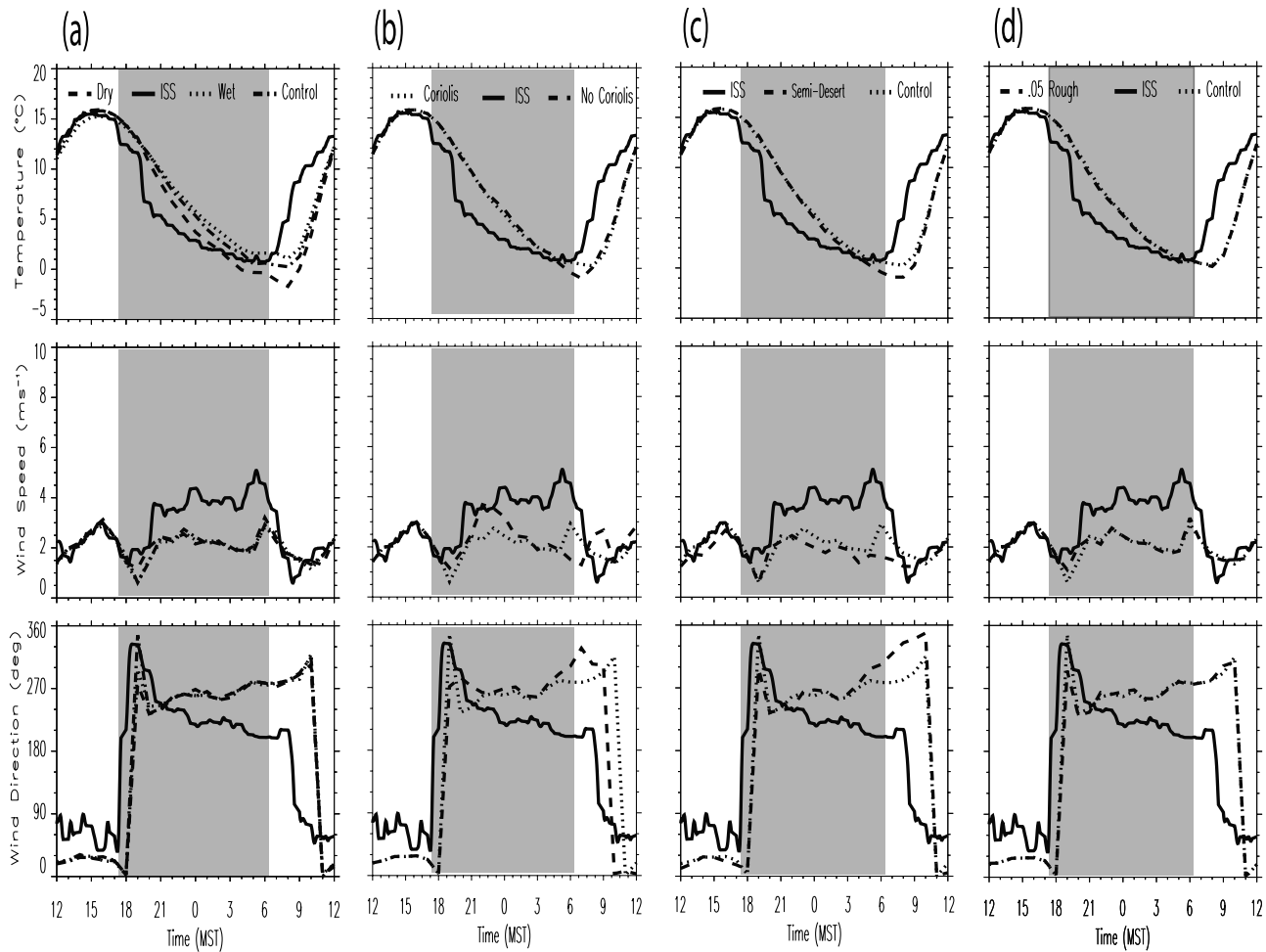
Figure 15. Simulated near surface temperature, wind speed, and direction for simulations with (a) change in soil moisture content, (b) Coriolis and no Coriolis, (c) change in land cover, (d) change in surface roughness for IOP 5 22–23 October.

is typically neglected in analytical studies, because downslope flows frequently occur at a local scale (∼10 km). In the control simulation, Coriolis force was included throughout the simulation. In the sensitivity run, the Coriolis force was turned off just before sunset at 1800 LST to allow the nighttime phase to develop without the influence of the Coriolis force. One goal of this experiment was to determine to what degree the nocturnal near-surface wind maximum could be attributed to inertial oscillations that produce nocturnal low-level jets.

[32] Figure 15 shows time series of near-surface properties at the ISS site for different soil moisture, land cover, surface roughness, and both with and without the Coriolis force. There are noticeable differences in the simulated near-surface temperatures when different soil moisture values were used in the simulations, with a larger temperature drop at night in the dry case than in the wet case, as expected. The differences in simulated near surface wind, however, are very small. The downslope winds for each simulation remain 1 m s^{-1} smaller than observations and the morning and evening transition occurred at nearly the same time in all three simulations. Figure 16 illustrates the impact of soil moisture on the thermodynamics of the region by showing

the vertical profile difference between the wet and dry simulations. As to be expected, the main variation between the simulations occurs in the strength of the surface inversion, where the dry case is stronger than the wet case. When semidesert land use is applied to the entire study region, the differences in wind direction are noticeable, but differences in temperature are smaller than those due to soil moisture change. The small temperature change at the ISS site may be because the changes in land use between the sensitivity and the control simulations are mostly over higher elevations; at the ISS site, the land use change is very small. The rougher surface provided little change from the control simulation. Wind speeds throughout the night were nearly identical, with exception to the afternoon transition periods, where the winds were slightly lower for the higher roughness simulation. Timing of the two transitional periods remained the same. Without Coriolis force, the downslope wind speeds are noticeably stronger and more variable throughout the nighttime period, and turn more to the west or even northwest rather than the southwestern direction observed during the period of downslope flow. The morning transition occurs one hour earlier without the Coriolis effect, which is closer to the observed transition. While there are more noticeable
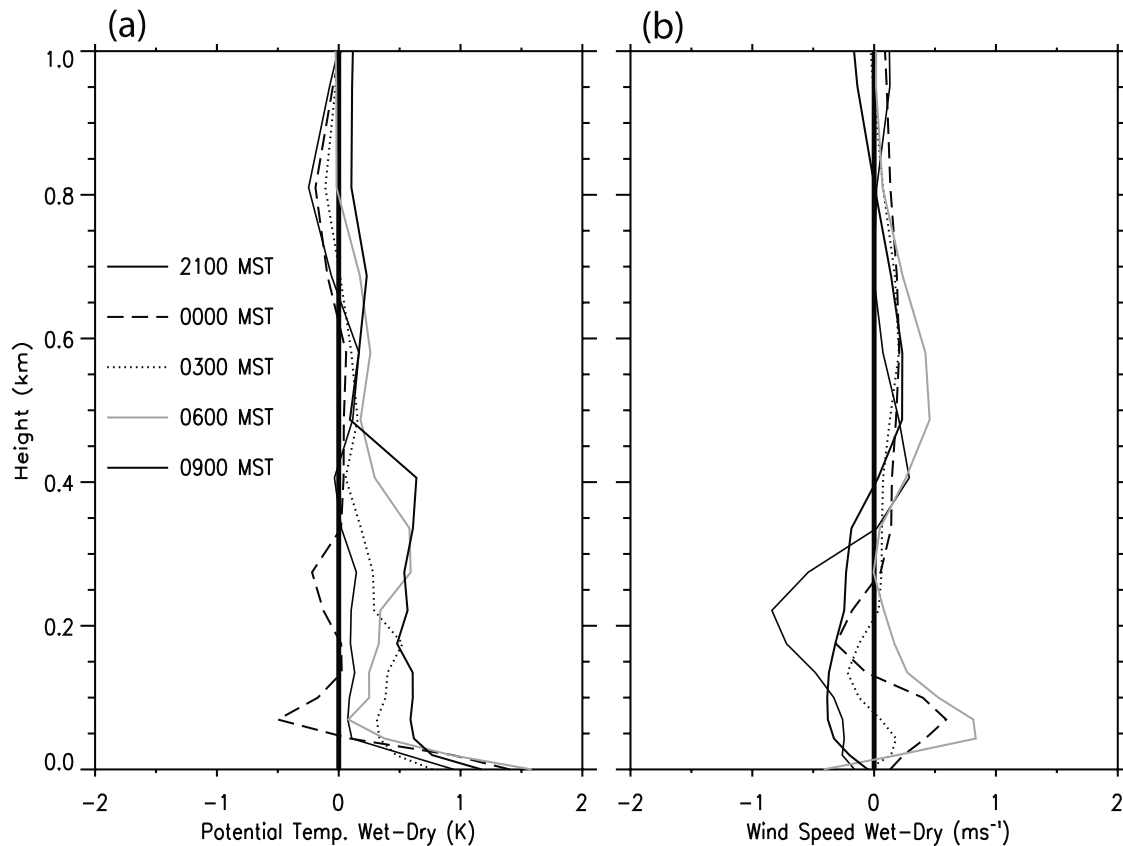
Figure 16. Difference of wet soil moisture case – dry soil moisture case for simulated (a) potential temperature, (b) wind speed for IOP 5 22–23 October.

differences in the Coriolis sensitivity study than the other studies, the differences are not significant, further suggesting that the observed low-level wind maximum is primarily a drainage flow, rather than the a low-level jet due to inertial oscillation of an ageostrophic wind component at the time of decoupling of the layer from the surface friction by the build up of the nocturnal inversion [*Blackadar*, 1957].

5. Conclusions

[33] Surface observations and frequent, high resolution upper air observations taken during the METCRAX field campaign in northern Arizona approximately 60 km east-southeast of Flagstaff were analyzed to characterize a regional-scale downslope flow and its relation to synoptic conditions and the ambient environment. The depth of this downslope flow is typically between 100 and 250 m with a peak speed of $4-6$ m s^{-1} occurring usually within the lowest 50 m above ground. Varying synoptic wind directions and speeds have large impacts on the downslope flow. Opposing ambient winds lead to longer period of evening transition, a shallower slope flow layer, and a smaller horizontal extent when compared to supporting synoptic winds. A simple analytical solution assuming local equilibrium appears to agree reasonably well with the observed average wind speed across the downslope flow layer, but the Prandtl solution for maximum downslope wind speed exhibits poor agreement with the observed maximum wind speed, especially in the case of quiescent conditions when local radiational cooling produces very large near-surface temperature deficits.

[34] The data analyses were augmented by high-resolution mesoscale numerical simulations using the RAMS model. The model simulations agree reasonably well with the slope flow observations. The simulation results suggest that the observed downslope wind is part of a regional-scale circulation that converges from high terrain of the Colorado Plateau toward the Little Colorado River Valley at night and diverges out of the river valley toward higher terrain during the day. Sensitivity simulations were performed to examine the effect of soil moisture, land use, surface roughness, and Coriolis force on the properties of the downslope flow in the region. Changes in soil moisture had little impact on simulated downslope wind properties, although relatively large difference in near-surface temperature was produced. The land cover change, which was mostly limited to high elevation, exhibited small effect on downslope wind direction. Surface roughness also exhibited negligible effects, with weaker winds during the afternoon transition of the higher surface roughness ($z_0 = 0.05$ m) simulation. Neglecting Coriolis force, as is typically done in idealized studies of small scale slope flows, had a more noticeable effect on the speed, direction, and transition of this regional scale downslope flow, but was still insignificant in the change of characteristics indicating the observations are from a drainage flow.

References

Alexandrova, O. A., D. L. Boyer, J. R. Anderson, and H. J. S. Fernando (2003), The influence of thermally driven circulation on PM10 concentration in the Salt Lake Valley, *Atmos. Environ.*, *37*, 421–437.

Arritt, R., and R. Pielke (1986), Interactions of nocturnal slope flows with ambient winds, *Boundary Layer Meteorol.*, *37*, 183–195.

Ball, F. K. (1956), The theory of strong katabatic winds, *Aust. J. Phys.*, *9*, 373–386.

Banta, R. M., and P. T. Gannon (1995), Influence of soil-moisture on simulations of katabatic flow, *Theor. Appl. Climatol.*, *52*, 85–94.

Berg, L. K., and S. Y. Zhong (2005), Sensitivity of MM5-simulated boundary layer characteristics to turbulence parameterizations, *J. Appl. Meteorol.*, *44*, 1467–1483.

Blackadar, A. K. (1957), Boundary layer wind maximum and their significance for the growth of nocturnal inversions, *Mon. Weather Rev.*, *38*, 283–290.

Chen, C., and W. R. Cotton (1983), A one-dimensional simulation of the stratocumulus-capped mixed layer, *Boundary Layer Meteorol.*, *25*, 289–321.

Clements, C. B., C. D. Whiteman, and J. D. Horel (2003), Cold air pool structure and evolution in a mountain basin: Peter Sinks, Utah, *J. Appl. Meteorol.*, *42*, 752–768.

Doran, J. C., J. D. Fast, and J. Horel (2002), The VTMX 2000 campaign, *Bull. Am. Meteorol. Soc.*, *83*, 537–551.

Fast, J. D., and S. Zhong (1998), Meteorological factors associated with inhomogeneous ozone concentrations within the Mexico City basin, *J. Geophys. Res.*, *103*, 18,927–18,946.

Fernando, H. J. S., M. Princevac, J. C. R. Hunt, and C. Dumitresu (2006), Katabatic flow over long slopes: Velocity scaling, flow pulsations and effects of slope discontinuities, paper presented at 12th Conf. on Mountain Meteorology, Am. Meteorol. Soc., Santa Fe, New Mexico.

Fitzjarrald, D. R. (1984), Katabatic wind in opposing flow, *J. Atmos. Sci.*, *41*, 1143–1158.

Haiden, T., and C. D. Whiteman (2005), Katabatic flow mechanisms on a low-angle slope, *J. Appl. Meteorol.*, *44*, 113–136.

Heinemann, G., and T. Klein (2002), Modelling and observations of the katabatic flow dynamics over Greenland, *Tellus Dyn. Meteorol. Oceanogr.*, *54*, 542–554.

Horst, T. W., and J. C. Doran (1986), Nocturnal drainage flow on simple slopes, *Boundary Layer Meteorol.*, *3*, 263–286.

Kondo, J., and T. Santo (1988), A simple model of drainage flow on a slope, *Boundary Layer Meteorol.*, *43*, 103–123.

Louis, J. F. (1979), A parametric model of vertical eddy fluxes in the atmosphere, *Boundary Layer Meteorol.*, *17*, 187–202.

Mahrt, L. (1982), Momentum balance of gravity flows, *J. Atmos. Sci.*, *39*, 2701–2711.

Manins, P. C., and B. L. Sawford (1979), A model of katabatic winds, *J. Atmos. Sci.*, *36*, 619–630.

McCumber, M. C., and R. A. Pielke (1981), Simulation of the effects of surface fluxes of heat and moisture in a mesoscale numerical-model: 1. Soil layer, *J. Geophys. Res.*, *86*, 9929–9938.

Mellor, G. L., and T. Yamada (1982), Development of a turbulence closure-model for geophysical fluid problems, *Rev. Geophys.*, *20*, 851–875.

Monti, P., H. J. S. Fernando, M. Princevac, W. C. Chan, T. A. Kowalewski, and E. R. Pardyjak (2002), Observations of flow and turbulence in the nocturnal boundary layer over a slope, *J. Atmos. Sci.*, *59*, 2513–2534.

Nappo, C. J., and S. K. Rao (1987), A model study of pure katabatic flows, *Tellus Dyn. Meteorol. Oceanogr.*, *39*, 61–71.

Pielke, R. A., et al. (1992), A comprehensive meteorological modeling system - RAMS, *Meteorol. Atmos. Phys.*, *49*, 69–91.

Poulos, G. S., J. E. Bossert, T. B. Mckee, and R. A. Pielke (2000), The interaction of katabatic flow and mountain waves. part I: Observations and idealized simulations, *J. Atmos. Sci.*, *57*, 1919–1936.

Prandtl, L. (1942), Führer durch die Sromungslehre, pp. 367-375, Vieweg-Verlag, Braunschweig, in *English as Prandtl's Essential of Fluid Mechanics*, edited by H. Oertel, pp. 723, Springer.

Raga, G. B., D. Baumgardner, G. Kok, and I. Rosas (1999), Some aspects of boundary layer evolution in Mexico City, *Atmos. Environ.*, *33*, 5013–5021.

Renfrew, I. A., and P. S. Anderson (2006), Profiles of katabatic flow in summer and winter over Coats Land, Antarctica, *Q. J. R. Meteorol. Soc.*, *132*, 779–802.

Shapiro, A., and E. Fedorovich (2007), Katabatic flow along a differentially-cooled sloping surface, *J. Fluid Mech.*, *571*, 149–175.

Smith, C. M., and E. D. Skyllingstad (2005), Numerical simulation of katabatic flow with changing slope angle, *Mon. Weather Rev.*, *133*, 3065–3080.

Smith, R., et al. (1997), Local and remote effects of mountains on weather: Research needs and opportunities, *Bull. Am. Meteorol. Soc.*, *78*, 877–892.

Soler, M. R., C. Infante, P. Buenestado, and L. Mahrt (2002), Observations of nocturnal drainage flow in a shallow gully, *Boundary Layer Meteorol.*, *105*, 253–273.

Sun, H., T. L. Clark, R. B. Stull, and T. A. Black (2006), Two-dimensional simulation of airflow and carbon dioxide transport over a forested mountain. part I: Interactions between thermally-forced circulations, *Agric. Forest Meteorol.*, *140*, 338–351.

Van Der Avoird, E., and P. G. Duynkerke (1999), Turbulence in a katabatic flow, *Boundary Layer Meteorol.*, *92*, 37–63.

Wang, J. X. L., and J. K. Angell (1999), Air stagnation climatology for the United States (1948–1998), Air stagnation climatology for the United States (1984-1998), NOAA/Air Resources Laboratory ATLAS No. 1., 1–6. (available at http://www.arl.noaaa.gov/pubs/online/atlas.pdf)

Whiteman, C. D. (1982), Breakup of temperature inversions in deep mountain valleys. part I: Observations, *J. Appl. Meteorol.*, *21*, 270–289.

Whiteman, C. D., and S. Zhong (2008), Downslope flows in a low-angle slope and their interactions with valley inversions. part I: Observations, *J. Appl. Meteorol. Clim.*, *47*, 2023–2038.

Zhong, S., and J. Fast (2003), An evaluation of the MM5, RAMS, and Meso-Eta models at subkilometer resolution using VTMX field campaign data in the Salt Lake Valley, *Mon. Weather Rev.*, *131*, 1301–1322.

Zhong, S., and C. D. Whiteman (2008), Downslope flows in a low-angle slope and their interactions with valley inversions. part II: Numerical modeling, *J. Appl. Meteorol. Clim.*, *47*, 2039–2057.

————————————

W. J. O. Brown and T. W. Horst, Earth Observing Laboratory, National Center for Atmospheric Research, P.O. Box 3000, Boulder, CO 80301, USA.

L. C. Savage III, W. Yao, and S. Zhong, Department of Geography, Michigan State University, 116 Geography Building, East Lansing, MI 48824, USA. (zhongs@msu.edu)

C. D. Whiteman, Department of Meteorology, University of Utah, Salt Lake City, UT 84112, USA.